Gutiérrez-Ch, J. G., Melentijevic, S., Senent, S., & Jimenez, R. (2025). DEM modelling of shaft load transfer behavior of rock-socketed piles. Computers and Geotechnics, 181, 107149. https://doi.org/10.1016/j.compgeo.2025.107149 © 2025 Elsevier Ltd

# DEM MODELLING OF SHAFT LOAD TRANSFER BEHAVIOR OF ROCK-SOCKETED PILES

**Gutiérrez-Ch J.G.[1*], Melentijevic S.[2**], Senent S.[3*] and Jimenez R.[4*]**

## ABSTRACT

The behavior of rock-socketed piles (RSPs) has been the aim of extensive research through field load tests, centrifuge tests, numerical simulations, etc. In this work, the Distinct Element Method (DEM) is employed to study the load transfer behavior at the shaft of rough rock-socketed piles (RSPs) and the effect of socket roughness on their load capacity and on their complex load transfer mechanisms (LTMs). DEM numerical results indicate that socket roughness crucially affects the load transfer behavior of RSPs, as illustrated by the investigation of the following aspects: (i) load-settlement response, (ii) inter-particle force distributions obtained by the DEM model of RSP tests, (iii) the evolution of stresses at the pile-rock interface (PRI) as a function of socket head settlement, (iv) the distribution of axial load and shaft resistance mobilized with depth, and (v) the failure mechanism. Numerical results highlight that an “arching effect” controls the shaft LTM of rough RSPs. This behavior occurs because the pile load is not uniformly distributed along its length, but transferred through the front of asperities at the PRI. Additionally, this work identifies that “measurement slices” rather than “measurement spheres”, provide a more accurate force distributions along the pile in DEM simulations. Furthermore, DEM results are compared with experimental and numerical published in the literature and good agreement is found. Finally, based on DEM results, an idealized shaft LTM for axially loaded RSPs is proposed. This mechanism enhances the understanding of the fundamental physical processes governing the shaft LTM of RSPs.

[1]Associate Professor. E-mail: jg.gutierrez@upm.es
[2]Associate Professor. E-mail: svmelent@ucm.es
[3]Associate Professor. E-mail: s.senent@upm.es
[4]Full Professor. E-mail: rafael.jimenez@upm.es
[*]Escuela Técnica Superior de Ingenieros de Caminos, Canales y Puertos Universidad Politécnica de Madrid. C/Prof. Aranguren, 3, Madrid 28040, Spain
[**]Facultad de Ciencias Geológicas, Universidad Complutense de Madrid. C/José Antonio Novais, 12, Madrid 28040, Spain

**Keywords** Rock-socketed piles (RSPs), shaft resistance, socket roughness, pile-rock interface (PRI), load transfer mechanism (LTM), Distinct Element Method (DEM).

[1]Associate Professor. E-mail: jg.gutierrez@upm.es
[2]Associate Professor. E-mail: svmelent@ucm.es
[3]Associate Professor. E-mail: s.senent@upm.es
[4]Full Professor. E-mail: rafael.jimenez@upm.es
[*]Escuela Técnica Superior de Ingenieros de Caminos, Canales y Puertos Universidad Politécnica de Madrid. C/Prof. Aranguren, 3, Madrid 28040, Spain
[**]Facultad de Ciencias Geológicas, Universidad Complutense de Madrid. C/José Antonio Novais, 12, Madrid 28040, Spain

## Highlights

- The Distinct Element Method is employed to study the load transfer behavior at the shaft of rough rock-socketed piles.
- The effect of socket roughness on the load capacity of rough rock-socketed piles and on their complex load transfer mechanisms is analyzed.
- The “arching effect” controlling the shaft load transfer mechanism from the pile to the surrounding rock is emphasized.
- An idealized shaft load-transfer mechanism of rough rock-socketed piles is proposed.

[1]Associate Professor. E-mail: jg.gutierrez@upm.es
[2]Associate Professor. E-mail: svmelent@ucm.es
[3]Associate Professor. E-mail: s.senent@upm.es
[4]Full Professor. E-mail: rafael.jimenez@upm.es
[*]Escuela Técnica Superior de Ingenieros de Caminos, Canales y Puertos Universidad Politécnica de Madrid. C/Prof. Aranguren, 3, Madrid 28040, Spain
[**]Facultad de Ciencias Geológicas, Universidad Complutense de Madrid. C/José Antonio Novais, 12, Madrid 28040, Spain

## 1. Introduction

Shaft resistance is crucial for the load transfer mechanism (LTM) of axially loaded rock-socketed piles (RSPs) because it is mobilized first, hence dominating the pile's serviceability requirement associated to its maximum allowable settlement (typically around 1% of its diameter; Whitaker and Cooke 1966). For this reason, the LTM and the shear behavior of pile-rock interfaces (PRIs) have been studied for many years.

Based on laboratory and field load tests, Pells et al. (1980), Williams and Pells (1981), Horvath et al. (1983), and Rowe and Armitage (1984), indicated that several factors affect the shaft resistance of RSPs: e.g., the socket roughness, the socket length and its diameter, the type and quality of the rock mass, etc. Furthermore, field load tests and numerical models conducted by Seidel and Haberfield (1995) and by Hassan and O'Neill (1997), respectively, direct shear tests on rock-concrete interfaces by Gu et al. (2003) and Krounis et al. (2016), and small-scale load tests by Dai et al. (2017), confirmed that socket roughness and normal stiffness at pile-rock interfaces (PRIs) are critical factors to reproduce the shaft behavior of RSPs. Similarly, Gutiérrez-Ch et al. (2020a; 2021b) demonstrated that centrifuge tests with Fiber Bragg grating sensors can be employed to investigate the LTM of RSPs. More recently, Murali et al. (2022) and Zhao et al. (2024) analyzed the load-bearing mechanism (at the asperity level) of RSPs through small-scale load tests and the rock fragmentation method, respectively. Additionally, full-scale field tests conducted on RSPs in conglomerated rock mass by Skejić et al. (2022) confirm that roughness at the PRI affects the load transfer response of RSPs.

59 The laboratory and field tests described above did not produce a detailed framework
60 to characterize the shaft LTM of RSPs, also involving difficulties and high costs
61 associated to experimental efforts. These disadvantages have drawn attention to the
62 alternative use of numerical methods, such as the Distinct Element Method (DEM),
63 the Finite Element Method (FEM) or the Finite Difference Method (FDM). Previous
64 studies employing the FEM (see e.g., Hassan and O'Neill 1997; Melentijevic and
65 Olalla 2014; Gutiérrez-Ch and Melentijevic 2016) provided insight regarding the
66 effect of roughness on the socket's shaft resistance, and on its LTM. Similarly, the
67 DEM approach was employed by Bahaaddini et al. (2013) and Gutiérrez-Ch et al.
68 (2018) to simulate rock-rock and rock-concrete interfaces with different degrees of
69 roughness. In addition, Gutiérrez-Ch (2020) and Gutiérrez-Ch et al. (2020b, 2021a)
70 used DEM simulations to estimate the shaft resistance of rough RSPs, showing that
71 DEM models can reproduce important aspects of the interface behavior –e.g.,
72 dilation, failure of asperities, etc.–. However, a deeper understanding about how
73 socket roughness influences the load transfer behavior (i.e., on how load is
74 transferred to the surrounding rock, due to an "arching effect" affects the shaft
75 resistance distribution along the pile, its axial load, and the stress distribution within
76 the pile) and the failure mechanism of RSPs is still needed.

77 To that end, this paper expands the Author's previous works (see Gutiérrez-Ch et
78 al., 2020b, 2021a-b for details) on this topic, by conducting DEM analyses that help
79 us to gain new knowledge on the load-transfer behavior at the shaft of RSPs with
80 different degrees of socket roughness. The novelty of this paper lies in several key
81 aspects that contribute to a deeper understanding of RSPs behavior: (1) a

comprehensive analysis is presented, detailing all stages of the load-settlement response (pre-peak, peak and post-peak) for axially loaded RSPs, (2) an in-depth investigation of the pile LTM to the surrounding rock is conducted. This includes exploring the "arching effect" and its role in governing the LTM from the pile shaft to the rock, a concept that has not been fully explored in this context. Also, the behavior of the "arching effect" is further analyzed by considering stress components at the PRI. Then, (3) an innovative method that uses “measurement slices” rather than conventional “measurement spheres” in DEM models, is introduced to analyze the LTM of RSPs, focusing on the axial load and shaft resistance mobilized along the pile, (4) a detailed failure mechanism of RSPs is presented, (5) DEM results are compared and validated against previous studies, demonstrating that the DEM simulations reproduce well the overall trends observed in existing literature, and (6) a shaft LTM for RSPs that synthesizes previous theories with the key findings from this study is proposed.

## 2. 3D DEM simulation of RSP testing considering socket roughness

### 2.1 Fundamentals of DEM with PFC

Three-dimensional (3D) DEM models developed by the Particle Flow Code (PFC) (Itasca Consulting Group Inc., 2014) are employed in this work. In such DEM models, materials are represented as a discontinuous medium composed of rigid and finite-sized spherical particles with Uniform or Gaussian radii distributions, and with interactions and boundary conditions that are simulated using appropriate models. For instance, “walls” are employed to apply velocity boundary conditions to the particle’s assemblies, or to compact or confine them; similarly, walls and particles

105 can interact with one another through forces (and, in some cases moments) that
106 develop at their contacts. The system evolution is computed through explicit dynamic
107 application of Newton's second law to the particles, considering their force-
108 displacement law at the contacts; and mechanical interactions are created or
109 destroyed by a contact-detection algorithm (Itasca Consulting Group Inc. 2014).

110 PFC provides different "contact models" to simulate specific microstructural features,
111 and "interfaces" to reproduce the macroscopic behavior –i.e., failure and sliding
112 along interfaces, fracture and crack propagation, etc.– of intact materials. In this
113 research, the Flat-Joint Contact Model (FJCM) is employed to represent 3D bodies
114 involved in the tests (i.e., the concrete of the pile and the rock around it); whereas
115 the Smooth-Joint Contact Model (SJCM) is employed to represent the behavior of
116 the PRI. Both contact models are selected based on their capabilities to reproduce
117 the macroscopic response of rock and concrete materials and their corresponding
118 interactions (Gutiérrez-Ch et al. 2018; 2020b). Rock and concrete properties –the
119 uniaxial compressive strength,$\sigma_c$, the Young's modulus,$E$, and the Poisson's ratio,
120 $\nu$– are listed in **Table 1**, and the calibrated micromechanical parameters of the FJCM
121 and of SJCM employed are listed in **Table 2** and **Table 3**, respectively. (The
122 calibration process was described in Gutiérrez-Ch et al. (2018, 2020b) and, for
123 brevity, is not repeated).

124

125

**Table 1.** Average values of rock properties

| Sample | Macro-properties | |
|---|---|---|
| Sandstone (S3) | $\sigma_c$ (MPa) | 21.77 |
| | $E$ (GPa) | 3.25 |
| | $\nu$ | 0.10 |
| Concrete | $\sigma_c$ (MPa) | 40 |
| | $E$ (GPa) | 29.95 |
| | $\nu$ | 0.20 |

Source: Data from Gu et al. (2003).

**Table 2.** Micro-mechanical properties of FJCM.

| | Sandstone-S3 | Concrete |
|---|---|---|
| Particle micromechanical properties | | |
| Effective modulus, $E^*$(GPa) | 1.90 | 27.00 |
| Normal-to-shear stiffness ratio of both particle and bond, $k^* = k_n/k_s$ | 1.45 | 2.75 |
| Friction angle ∅ (º) | 35 | 30 |
| Ball density, $\rho(kg/m^3)$ | 2550 | 2500 |
| Minimum radius, $R_{min}$ (mm) | 1.0 | 0.8 |
| $R_{max}/R_{min}$ | 1.4 | 1.5 |
| Flat-joint micromechanical properties | | |
| Effective modulus, $\overline{E^*}$(GPa) | 1.90 | 27.00 |
| Normal-to-shear stiffness ratio of both particle and bond, $\overline{k^*}$ | 1.45 | 2.75 |
| Cohesion, *c* (MPa) | 7.90 | 13.55 |
| Tensile strength, $\sigma_t$ (MPa) | 3.5 | 6.0 |

Source: Data from Gutiérrez-Ch et al. (2018).

**Table 3.** Micro-mechanical properties of SJCM.

| | Sandstone(S3)-Concrete |
|---|---|
| Joint normal stiffness, $k_{n\,SJ}$ (MPa/mm) | 10 |
| Joint shear stiffness, $k_{s\,SJ}$ (MPa/mm) | 5 |
| Joint coefficient of friction, $\mu_{SJ}$ ($\tan$ ∅ (º)) | 0.70 |
| Joint cohesion, $c_{SJ}$ (MPa) | 0 |

Source: Data from Gutiérrez-Ch et al. (2018).

## 2.2 Set-up of the numerical model

### *2.2.1 Generation of the 3D DEM RSP model*

Usually, DEM simulations are computationally expensive, especially when used to reproduce full-scale problems such as RSPs (see **Fig. 1**(a)). For instance, a previous work conducted by these Authors (Gutiérrez-Ch et al. 2021a) demonstrated that, for

DEM simulation of UCS tests, the computational time is increased 80 times when a 3D model is used instead of a 2D model. To reduce the computational cost, the 3D DEM model is elaborated considering the following assumptions: (i) a 45-degree angle model (instead of a full section) is used, (ii) the rock body is discretized using three zones with different particle size distributions, (iii) only the rock socket is considered, with pressure loads to simulate the self-weight of the pile ($Q_1 = 0.125$ MPa at the wall head rock) and of the soil stratum ($Q_2 = 0.1$ MPa at the wall head pile) overlying the rock-soil interface (see **Fig. 1** and **Fig. 2**), and (iv) the pile-rock interface is considered unbonded. Furthermore, the particle size distribution presented in **Fig. 2** is based on a previous sensitivity analysis conducted by the Authors (see Gutiérrez-Ch et al. (2021a) for details). Also, note that, to facilitate the discussion in Section 3, the regions of an asperity are also presented in **Fig. 1**(c).

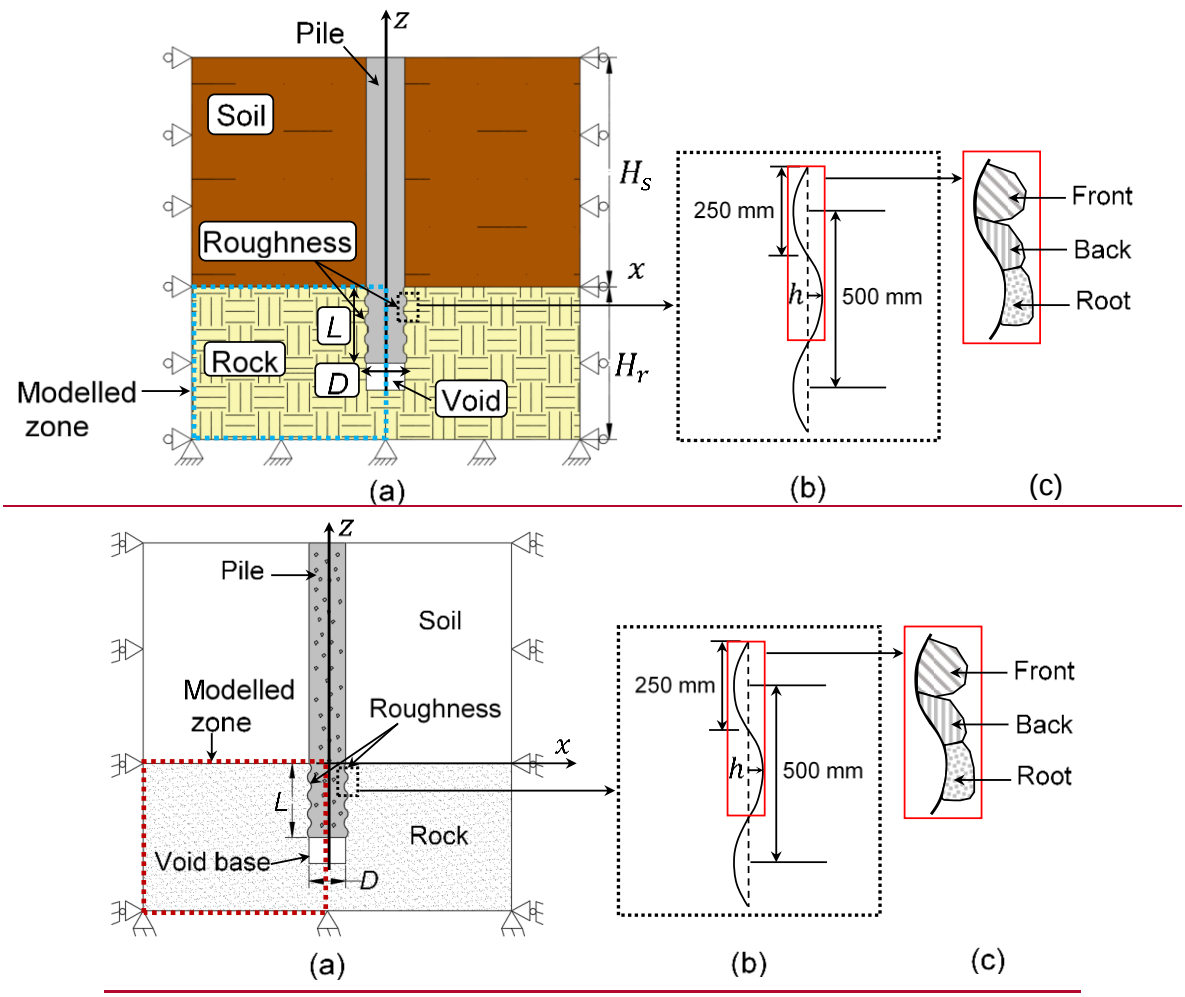


**Fig. 1.** Idealized rock-socketed pile: (a) cross-section of pile model in 2D, (b) roughness profile used at the PRI, (c) regions of an asperity.

The 3D RSP sample is generated under no-water conditions following the methodology proposed by Gutiérrez-Ch et al. (2019, 2020b), whose steps are summarized as follows: (i) initial random particle assembly of rock and pile bodies, (ii) application of an isotropic initial stress (around 1% of the $\sigma_c$ and considering a lateral earth pressure coefficient of $K_o = 1$) to obtain a better contact distribution during sample generation, (iii) elimination of floating particles, to guarantee that each particle has at least three contacts with its surrounding particles, (iv) application of the FJCM and SJCM models, with their calibrated micromechanical parameters

(listed in **Tables 2**-**3**), and (v) initialization of the in situ stresses by gravity load and application of the overburden loads involved in each test. (Note that $K_o = 1$ assumes that the soil above the rock layer is under at-rest stress conditions, and that the rock layer itself typically provides a more rigid interface than the overlying soil). The nominal socket length ($L$) and the nominal socket diameter ($D$) are both 0.8 m (i.e., $L/D = 1.0$) for all DEM models presented herein. The influence of the pile length and its diameter on the load transfer response of RSPs have not been considered in this work; however, a ratio of $L/D = 1.0$ is appropriate for RSP in medium to hard rocks as considered herein (Ng et al., 2001; Basarkar and Dewaikar, 2006; Rajan and Krishnamurthy, 2019). The bottom of the pile excavation is made void to eliminate the contribution of base resistance and to simulate conditions that may occur during pile installation (e.g., debris accumulated at the bottom of pile or rock with cavities (Seidel and Collingwood 2001)). This allows for more accurate simulations of the shaft load transfer behavior, particularly when assessing the impact of socket roughness and potential variations in load distribution. **Fig. 2** shows one 3D RSP model generated with the methodology described above.

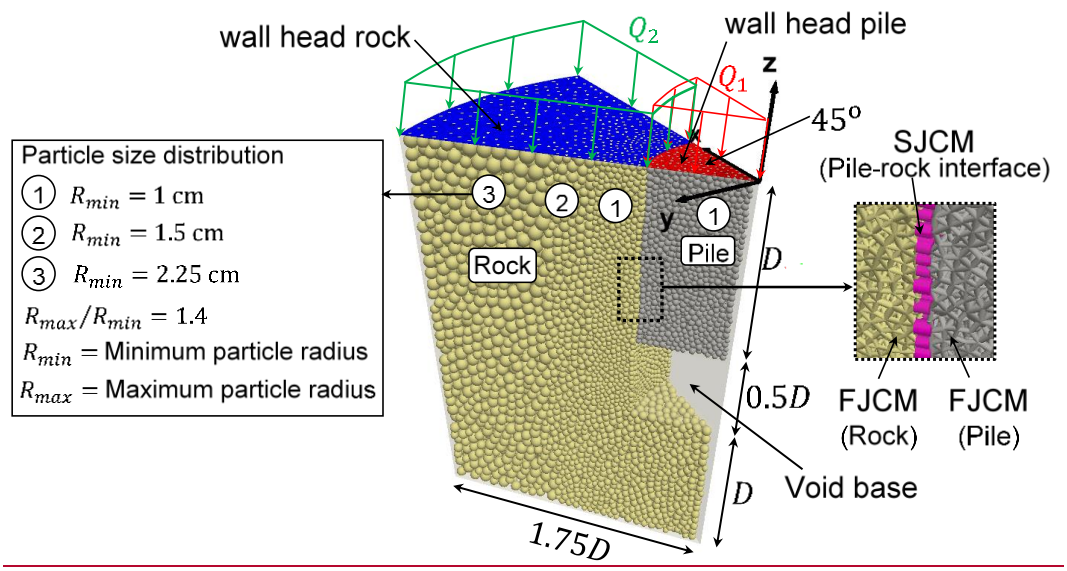


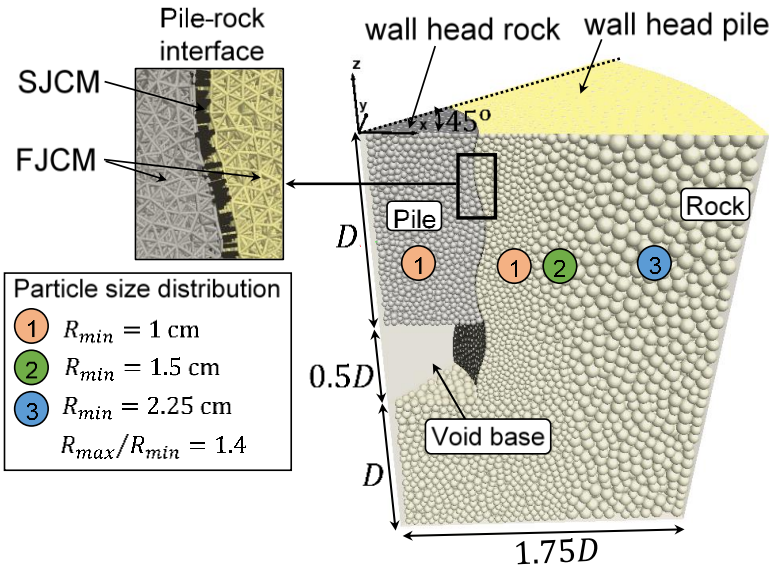


**Fig. 2.** Illustration of DEM model of the RSP considered, with information about contact models employed and about particle size distribution. ($R_{max}$ and $R_{min}$ represent the maximum and minimum particle radii, respectively).

*2.2.2 Pile-rock interface (PRI)*

Many researchers have analyzed the behavior of axially loaded RSPs considering PRIs with triangular asperities (Johnston et al. 1987; Kodikara and Johnston 1994; Gu et al. 2003; Xu et al. 2020); however, in this work, PRIs are simulated using sinusoidal surfaces, since it is the typical morphology expected in sockets drilled with

an auger tool (O'Neill et al.,1996) or with a core barrel tool (Skejić et al., 2022). In particular, to obtain different degrees of socket roughness, the PRI is modelled using sinusoidal asperities with amplitudes of $h = 4$, 10, 20, 32.5 and 40 mm, and with a wavelength of 250 mm in all models (see **Fig. 1**(b)). Hence, five RSP models with different levels of roughness are produced; they are denoted using their roughness factor ($RF$), defined by Horvath et al. (1983) as:

$$RF = \frac{h_m L_t}{RL} \tag{1}$$

where $h_m$ is the mean height (or amplitude) of asperities, $R$ is the nominal socket radius, $L_t$ is the total travel distance along the socketed wall, and $L$ is the nominal socket length. Given the geometries described above, the five models employed herein have $RF$ values of 0.010, 0.025, 0.050, 0.085 and 0.106, respectively. Such $RF$ values are in the range of socket roughness that could be obtained in "smooth" piles ($RF \leq 0.025$) or in "rough" piles ($RF > 0.025$) when standard tools, or special drilling tools, respectively, are employed (Gutiérrez-Ch et al. 2021b).

Finally, to conduct the numerical pile tests, the displacements ($u$) of the boundary walls at the bottom and side of the model are fixed ($u_x = u_y = u_z = 0$; where $u_x$, $u_y$ and $u_z$ represent displacement in $x$, $y$ and $z$ directions, respectively); whereas the axial load is applied to the wall representing the pile head using an axial displacement-controlled rate of 0.05 m/s, which is low enough to ensure that the model remains in quasi-static equilibrium –i.e., a loading rate low enough that does not develop significant dynamic effects that could affect the load-settlement response of the RSP–.

## 3. Results

### 3.1 Preliminary comments

As reported in Section 2.1, the micro-mechanical properties of the DEM RSP models developed herein were calibrated and validated through laboratory tests (UCS tests and direct shear tests) summarized in Gutiérrez-Ch et al. 2018). The comparison and validation of the load and shaft resistance-settlement response obtained from DEM models developed herein based on experimental data and formulations published in literature, were presented and discussed in Gutiérrez-Ch et al., 2020b, 2021a, showing strong alignment with previously published results; thus, in order not to repeat, it is not presented herein again. Hence, this research provides valuable new insights into the LTM of axially loaded RSPs. To the best of the Author's knowledge, these findings represent a comprehensive examination of this topic in the existing literature, thereby filling a gap and enhancing our understanding of LTM in axially loaded RSPs.

### 3.2 Load-settlement response

To illustrate the pre-peak, peak and post-peak behavior of RSPs for different $RF$, the pile axial load ($Q_z$) versus the socket head settlement ($\delta$) curves are employed as an example (see **Fig. 3**(a)). (The bearing capacity presented in **Fig. 3** is a partial estimation and it does not account for the contribution of the soil shaft resistance above the rock; or for other factors that may influence the total capacity in real conditions). As it can be observed, the roughness at the PRI increases the load capacity of RSPs and it also affects their pre-peak, peak and post-peak response; note that (i) the load capacity increases as the $RF$ increases during the pre-peak

stage, (ii) the settlement at peak load ($\delta_{peak}$) decreases as roughness increases, (iii) the post-peak behavior of "rougher" piles tends to be more ductile than for "smooth" piles, and (iv) there seems to be an upper limit after which further increasing the roughness no longer increases the peak load ($Q_{z,peak}$) capacity. These findings are aligned with centrifuge results reported by Gutiérrez-Ch et al. (2021b), where a similar response was experimentally measured in centrifuge tests for RSPs in a soft rock ($\sigma_c = 1.15$ MPa).

In addition, **Fig. 3**(b) shows the normalized axial load-settlement response, in which the $Q_z$ and $\delta$ values reported in **Fig. 3**(a) are normalized by their corresponding $Q_{z,peak}$ and $\delta_{peak}$ values. Results show that the normalized pre-peak behavior tends to be similar for "rough" piles (i.e., $RF > 0.025$), whereas slight variations are observed for "smooth" piles (i.e., $RF = 0.010$ and 0.025), which may be attributed to the interface shearing process; as shown in Section 3.4, the bonds between particles located at the vicinity of the PRI are broken earlier for "smooth" piles than for "rough" piles, so that such particles become "third bodies" that slightly and temporarily increase the PRI roughness (Xu et al., 2020); therefore, slight variations of the load-settlement response are observed for "smooth" piles.

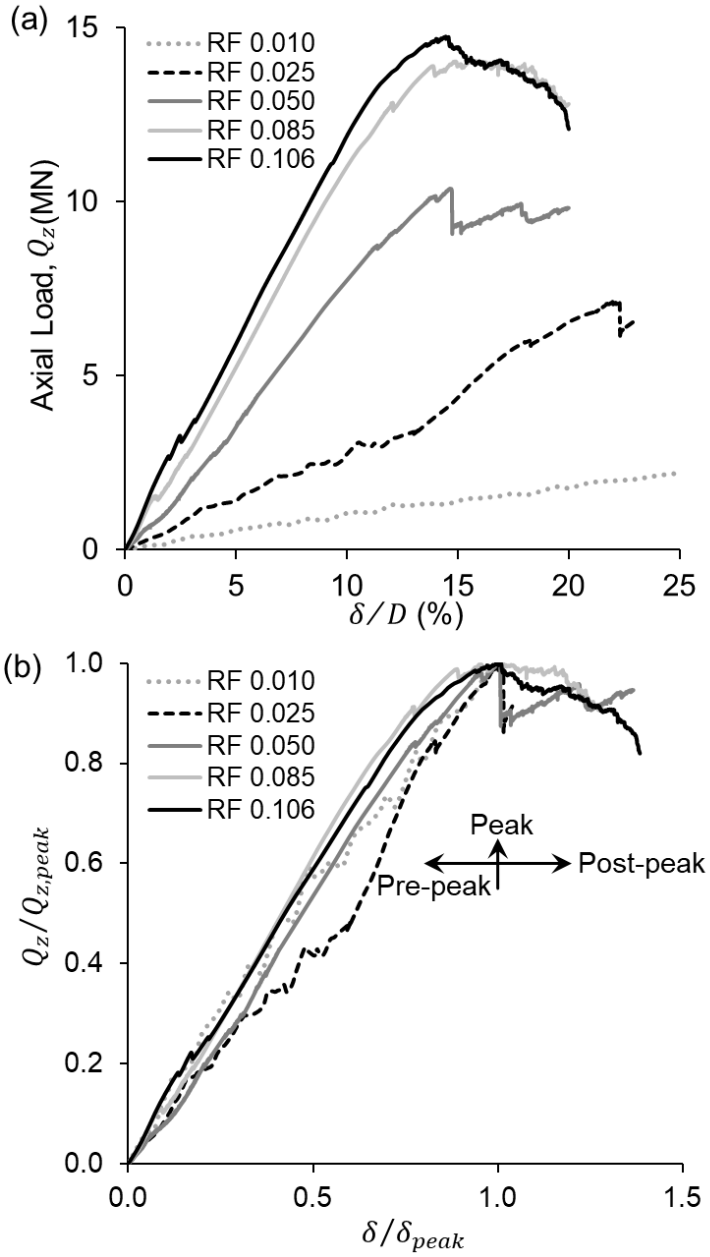


**Fig. 3.** Pre-peak, peak and post-peak behavior for RSPs for different $RF$: (a) load-settlement response, (b) normalized load-settlement response.

### 3.3 Load transfer mechanism

DEM models allow one to compute contact forces and their distributions, to track displacements of particles and to monitor bond breakages and micro-cracks

propagations, to compute stresses within a given zone, etc. Using such capabilities, the LTM of RSPs is analyzed.

*3.3.1 Identification of arching effect from inter-particle force distribution*

First, 3D views of inter-particle force distributions are employed (see **Fig. 4**, where the results correspond to RSPs with $RF = 0.050$ and 0.085; a similar trend is also obtained for other RFs). To facilitate the visualization, the rock and pile particles are made "transparent", and the PRI and the pile head have been highlighted with black and red color, respectively (see **Fig. 4**). Also, to facilitate the discussion, the inter-particle force distribution is presented at different $\delta$ (expressed as percentage of the equivalent pile diameter, $D$). At 'early' loading stages (e.g., for $\delta = 1\%D$, see **Fig. 4**) note that, (i) the transmission of forces from the pile to the rock mainly occurs at the front of the upper asperities, located closer to the RSP head, (ii) an "unloaded" area –or a region with reduced contact forces– forms at the back of asperities, and (iii) forces in the pile mainly concentrate in its upper portion, so that axial loads are not transmitted down to the lower portion of the pile (see **Fig. 4**). Upon further loading (i.e., for $\delta > 1\%D$), the force-chain loads continue to increase (e.g., the plots for $\delta = 3\%D$, see **Fig. 4**), and pile forces are transferred to the rock along a wider region at the front of asperities (see **Fig. 4**(b)).

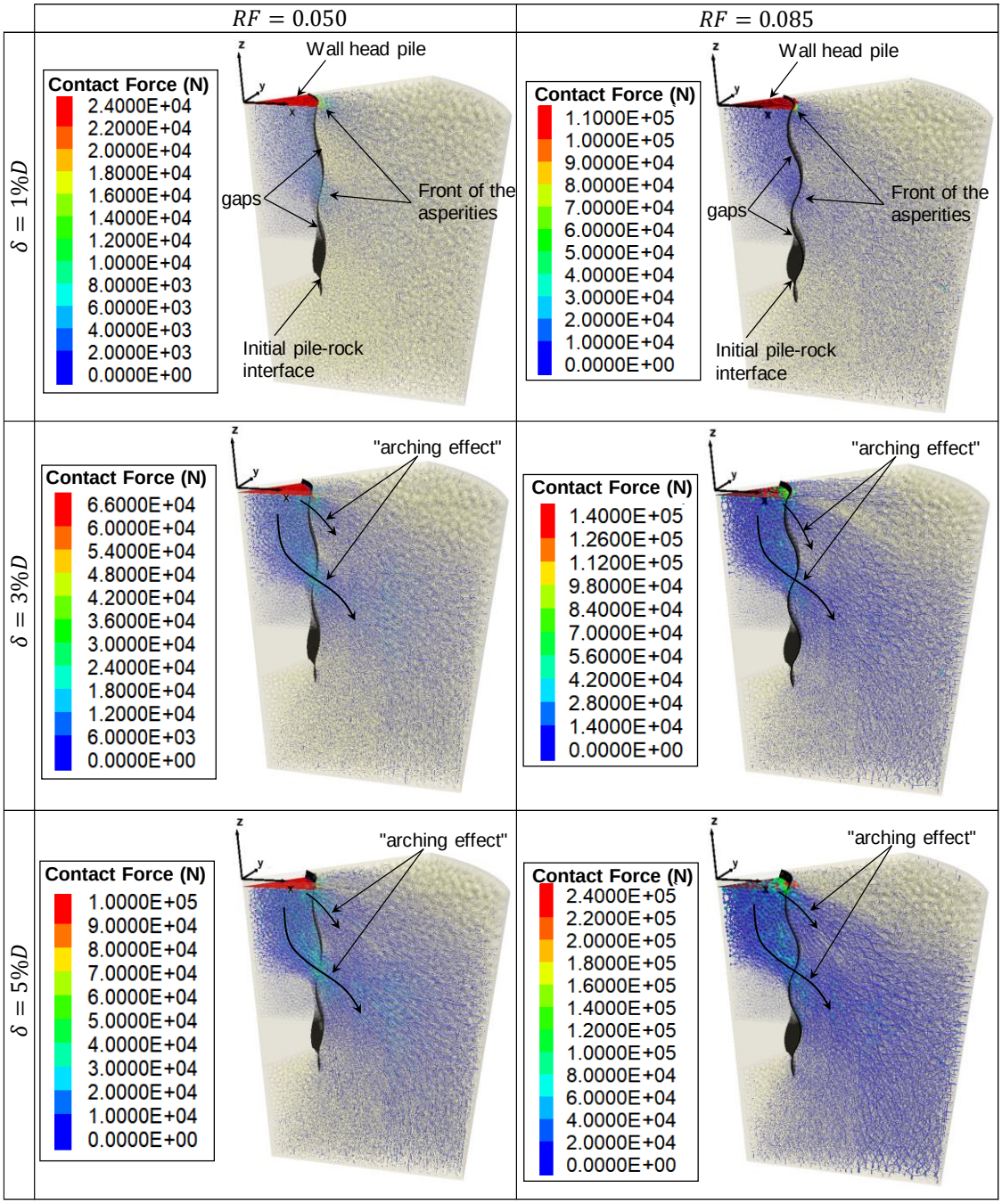


**Fig. 4.** Inter-particle force distribution with settlement for RSPs with $RF = 0.050$ and 0.085.

That is, we observe an “arching effect” that controls the Load Transfer Mechanism from the pile to the surrounding rock (see **Fig. 4**), suggesting that the LTM of “rough” piles are not homogeneous, so that their axial stress are mainly mobilized to the surrounding rock in the upper half of the pile. Furthermore, note that the backs of the

asperities continue to be relatively unloaded (in comparison with their fronts), and that this behavior continues to be similar for subsequent head settlements (e.g., for $\delta = 5\%D$, see **Fig. 4**). Therefore, the arching effect along the pile shaft occurs due to the development of a LTM between the pile and the surrounding rock. When a pile is subjected to axial load, the surrounding rock experiences a redistribution of stress, leading to the formation of an arching effect. Essentially, the load is not uniformly distributed along the pile length, but rather, a concentrated load is transferred through the front of the asperities, creating a load transfer arch. Furthermore, the arching effect reported herein may still occur if the pile in the numerical model is considered as a solid (instead of a DEM model consisting in spheres): Initial observations of this arching effect in the load transfer mechanism of rough rock-socketed piles were observed in shear stress distributions from FEM computations of rough piles socketed in sandstone and conglomerate, as reported by Gutiérrez-Ch (2020) and Skejić et al. (2022), respectively. Additionally, results suggest that boundary effects are negligible, as the force distribution is almost zero at the model boundaries.

*3.3.2 Analysis of the "arching effect" considering stress components at the PRI*

Next, the distribution of stress in the vicinity of asperities within the pile shaft is studied. To do that, thirty PFC3D measurement regions (MRs) were selected inside the rock body at different distances from the pile (denoted with numbers from 1 to 5, see **Fig. 5**), and at elevations corresponding to the front, back, and root of the "upper" and "lower" asperities (their exact locations are marked with red spheres in **Fig. 5**). Using such MRs, the axial ($\sigma_z$), radial ($\sigma_r$) and circumferential ($\sigma_\theta$) stress

components at each location are computed for each load step. The relationship between stress components and a normalized distance to the PRI (i.e., distance to PRI normalized by pile radius, or $d/R$), for different RSP head settlements, are shown in **Fig. 6** for the upper asperity and in **Fig. 7** for the lower asperity. (To facilitate the discussion, only RSP with $RF = 0.050$ is used.)

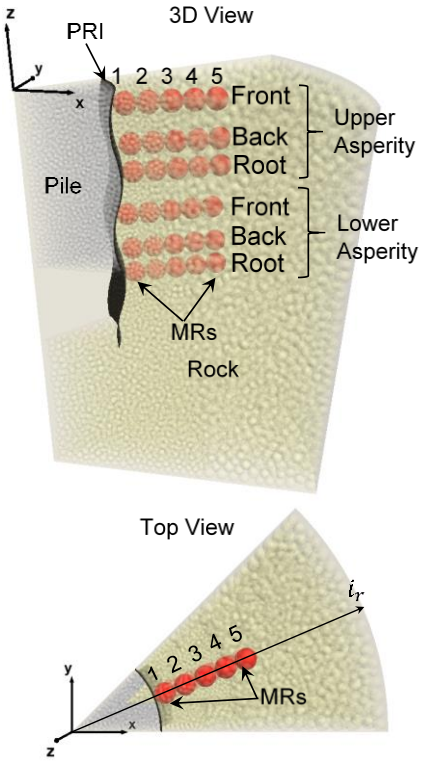


**Fig. 5.** Location of the measurement regions (MRs) in sections traced along the central radial line ($i_r$) at different depths of pile model (the red spheres represent the MRs).

**Fig. 6** – **Fig. 7** show that mainly compressive (negative) stresses occur at the front of both the lower and upper asperities for a wide range of settlement values considered ($\delta = 0 - 10\%D$). Initially, due to the arching effect discussed above (see Section 3.3.1), stress components for the MRs near the PRI (i.e., $d/R < 0.2$) at the back and at the root of the upper asperity are still close to zero for small settlements ($\delta = 1\%D$; see **Fig. 6**(b)-(c)). This suggests that the interface was initially unloaded

317 (similar to a gap forming at these parts of PRI) so that, after $\delta > 1\%D$, compression
318 stresses start to develop in all components due to pile downward displacement and
319 the pile transfers its pushing forces to areas closer to the back of the upper asperity,
320 as reported previously in the contact force distribution (see **Fig. 4** and **Fig. 6**(b)). A
321 similar trend occurs, for greater RSP head settlements, for stress components
322 recorded at the root of the upper asperity (see **Fig. 6**(c)).

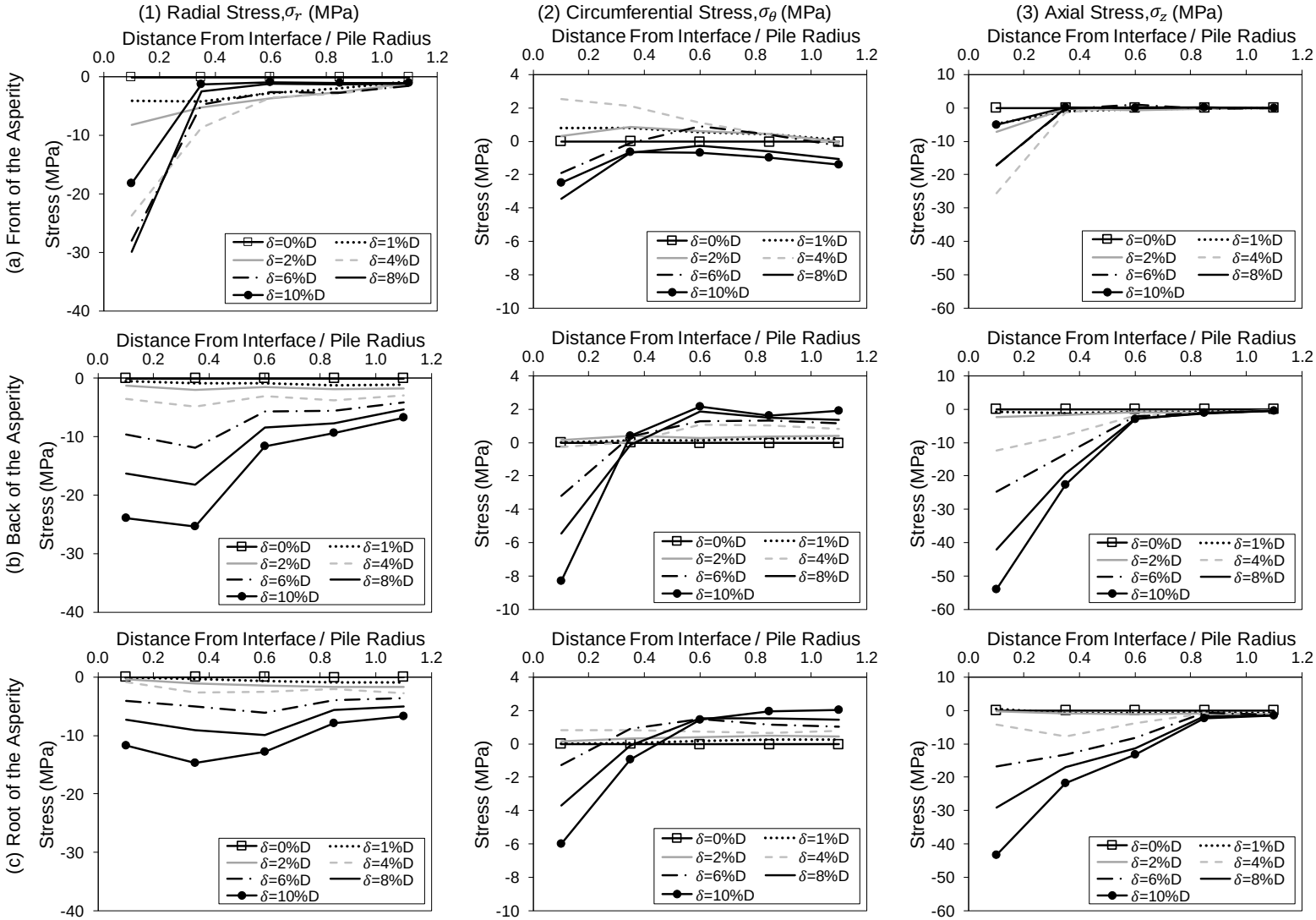


**Fig. 6.** Relationship between RSP head settlement and stress components along radial lines in the region around the upper asperity for RSP with $RF = 0.050$.

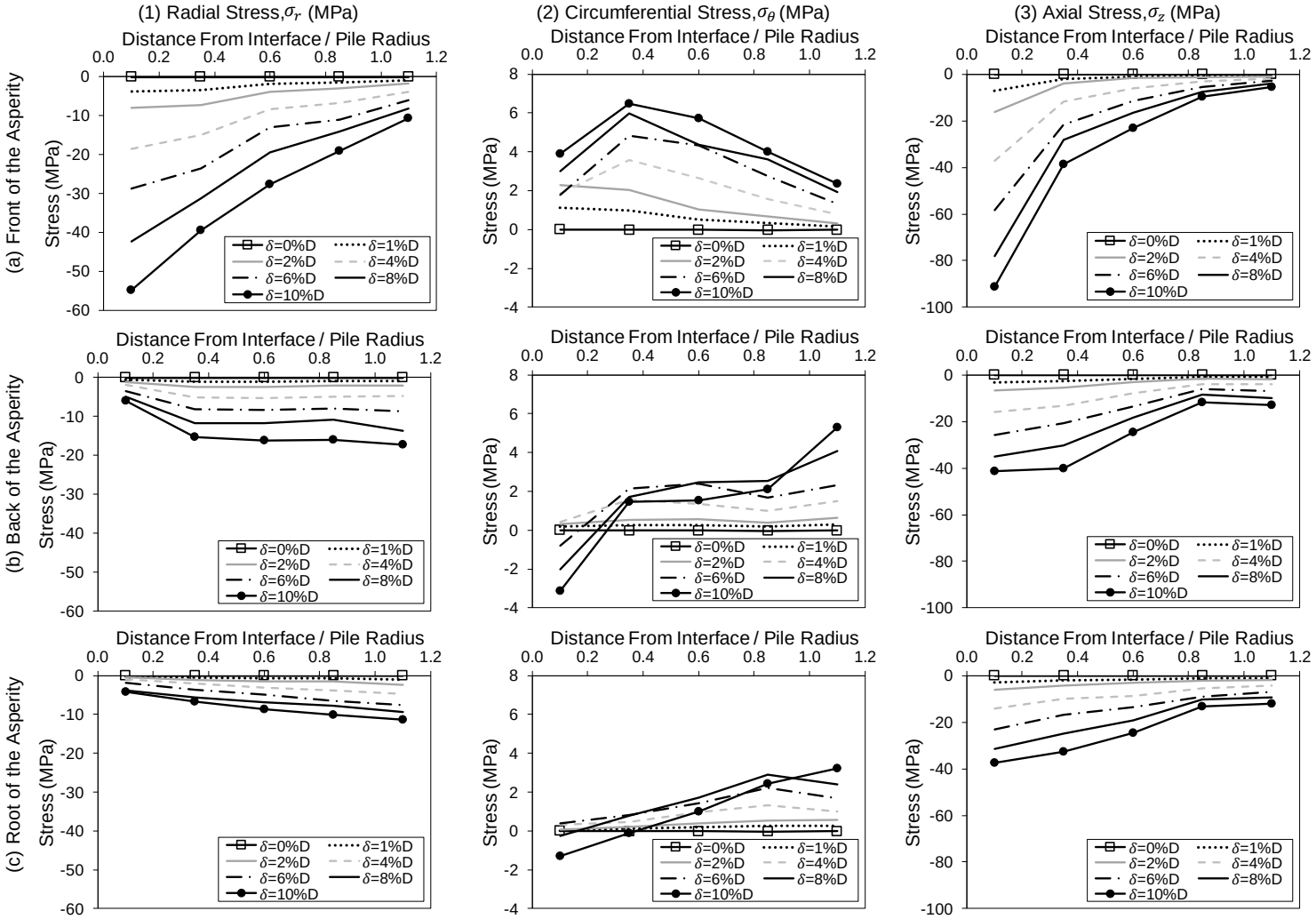


326

327 **Fig. 7.** Relationship between RSP head settlement and stress components along radial lines in the region around the lower asperity for RSP with
328 $RF = 0.050$.

Furthermore, $\sigma_z$ and $\sigma_r$ stresses at the front and at the root of the upper asperity are mostly mobilized up to $d/R \cong 0.4$ and 0.8, respectively (see **Fig. 6**(a1,a3) and **Fig. 7**(c1,c3)); whereas the $\sigma_\theta$ stress at the front of the upper asperity is mainly mobilized up to $d/R < 0.6$, and it evolves from tensile stress values for $\delta \leq 4\%D$ to compressive stress values for $\delta \geq 6\%D$ (see **Fig. 6**(a2)); note, however, that the $\sigma_\theta$ stresses at the back and at the root of such asperity do not change much with distance to the pile for $\delta \leq 4\%D$; for $\delta \geq 6\%D$, a transition occurs, from compressive stresses near the pile ($d/R \leq 0.4$) to tensile stresses further away from it ($d/R > 0.4$) (**Fig. 6**(b2,c2)).

Results discussed above support the "arching effect" idea reported in Section 3.3.1. That is, (i) most of the mobilized stresses in the LTM occurs at the front of the upper asperity for 'lower' socket head settlements, (ii) further pile settlements mobilize stresses at the back and root of the upper asperity, and at the front of the lower asperity (with greater mobilized stresses), and (iii) the stresses transferred from the pile to the surrounding rock decrease with increasing distance from the PRI (see **Fig. 6** – **Fig. 7**). These results agree with Hassan and O'Neill (1997), who reported results from FEM simulations showing that the load transfer from the pile to its surrounding rock mainly occurs within a distance from the interface equivalent to a pile radius; see **Fig. 6** – **Fig. 7**.

### *3.3.3 Analysis of the LTM using the axial load and shaft resistance distributions with depth*

This section studies, for piles with different $RF$, (i) the distribution with depth of their axial load ($Q_z$), and (ii) their distribution of unit shaft resistance ($\tau_s$). To that end, $Q_z$

at the pile head is computed as the force reaction recorded at the pile head wall of the DEM model, while $Q_z$ values deeper within the pile are computed multiplying the average stress at the pile cross-section computed at a given depth (i.e., using the same methodology that PFC3D uses for its spherical "measurement regions", but considering a "measurement slice" instead, see **Fig. 8**) times its nominal cross-section area. On the other hand, the $\tau_s$ at a given depth interval is computed as summation of the axial components of contact forces acting on particles at the pile-rock interface within such depth interval and dividing by its associated surface area (see **Fig. 8**).

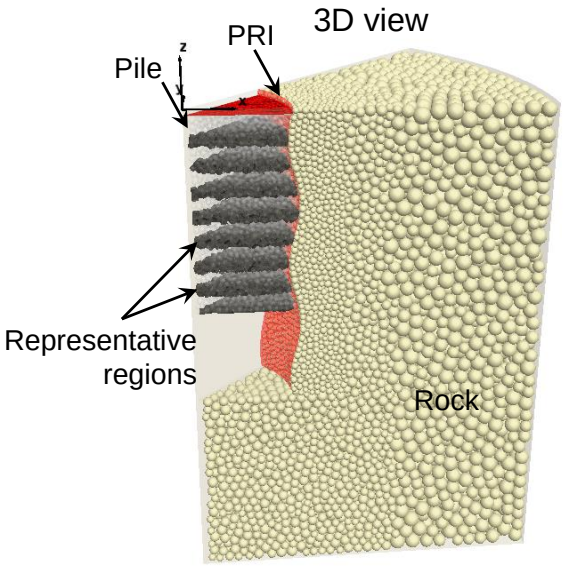


**Fig. 8.** Example of "measurement slices" to record axial stresses along the pile (model with $RF = 0.050$ and $\delta$=3%D).

Computed results of $Q_z$ and $\tau_s$ mobilized along the RSPs are shown, for different socket head settlements, in **Fig. 9** and **Fig. 10**. Note that, as discussed above, the "arching effect" associated to the LTM makes the shaft resistance to be mainly associated to the interface asperities, so that basically no load is transferred from the pile to the rock (i.e., the pile axial force is constant) within the region located,

approximately, between depths of 10-35 cm; i.e., coinciding with the depths where the back of the asperity is located, and down to the depth of the mid-root (see **Fig. 1**(c)).

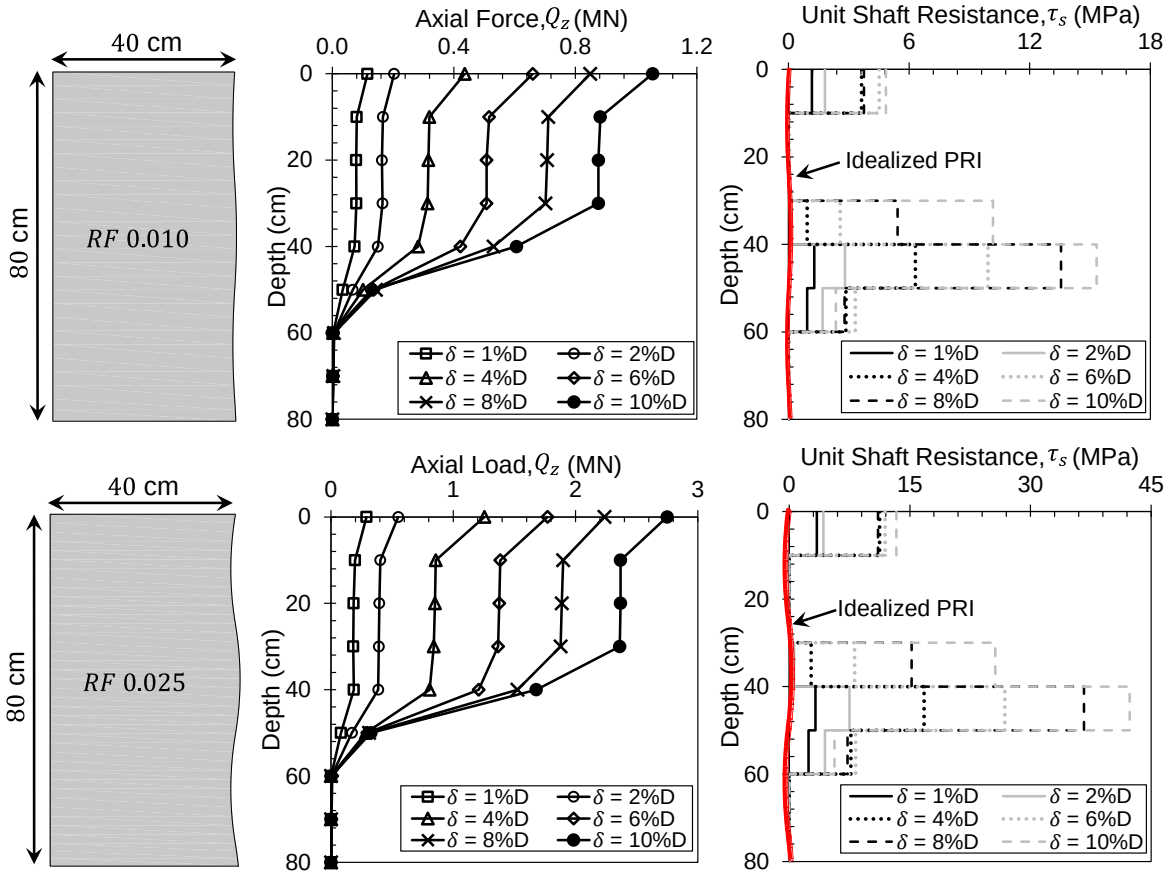


**Fig. 9.** Axial load ($Q_z$) and shaft resistance ($\tau_s$) distribution vs depth for 3D DEM RSP with $RF = 0.010$ and $0.025$ (the red line represents the idealized PRI to facilitate the illustration of $Q_z$ and $\tau_s$ mobilized at different regions of the upper and lower asperity).

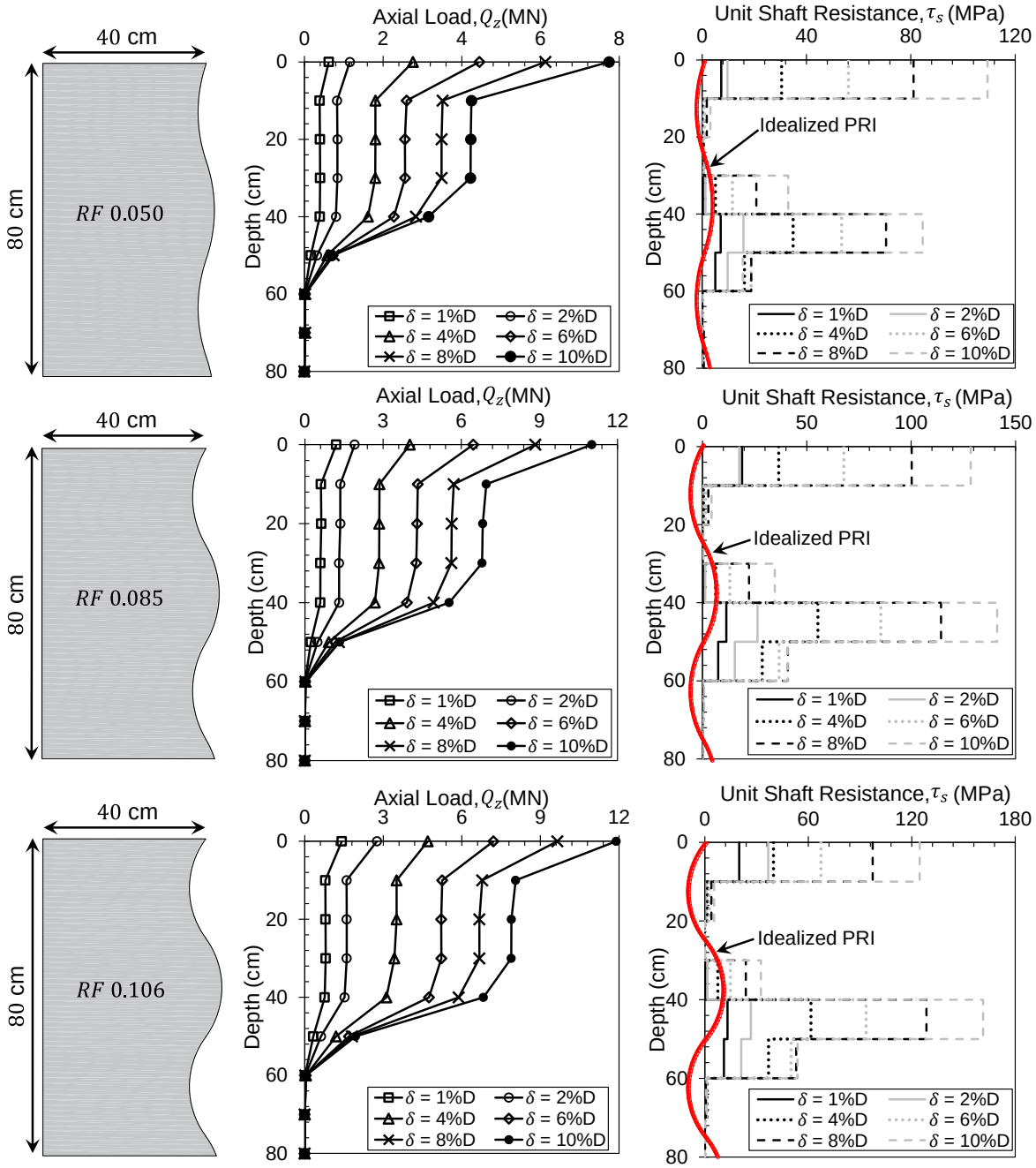


376

377 **Fig. 10.** Axial load ($Q_z$) and shaft resistance ($\tau_s$) distribution vs depth for 3D DEM RSP with $RF =$
378 $0.050$, $0.085$ and $0.106$ (the red line represents the idealized PRI to facilitate the illustration of $Q_z$
379 and $\tau_s$ mobilized at different regions of the upper and lower asperity).

380 Similarly, analyzing the inter-particle force distributions along different
381 "measurement slices" (see **Fig. 11**) shows that (i) their loads tend to decrease with
382 depth (as expected) and, due to the arching effect identified, (ii) that their

distributions along the pile cross-section are not uniform so that, for instance, they tend to concentrate in the outer region of the pile-cross section at depths of about 0 cm and 40-60 cm, hence coinciding with the fronts of asperities. Indeed, if one computes the pile's axial load by using just one "representative" measurement region within the pile, as illustrated in **Fig. 12**(a), this produces the mistaken result that pile loads reduce with depth in regions where almost no shaft resistance has been developed, see **Fig. 12**(b).

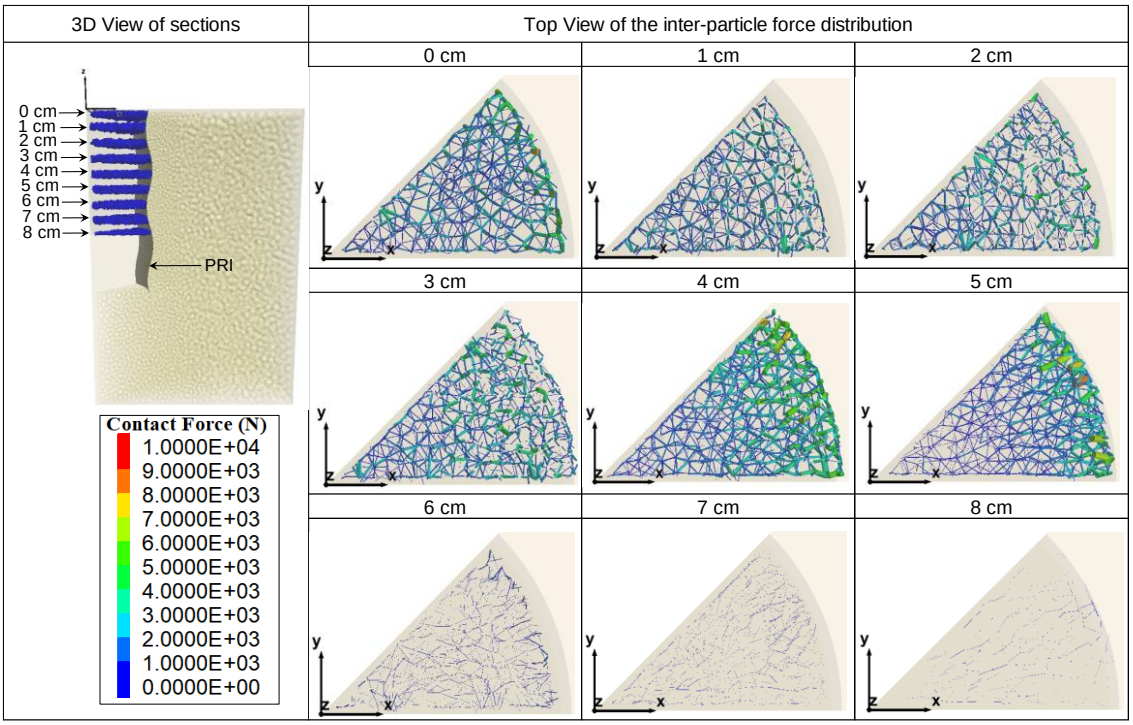


**Fig. 11.** Inter-particle force distribution for RSP with $RF = 0.050$, socketed and $\delta = 1\%D$.

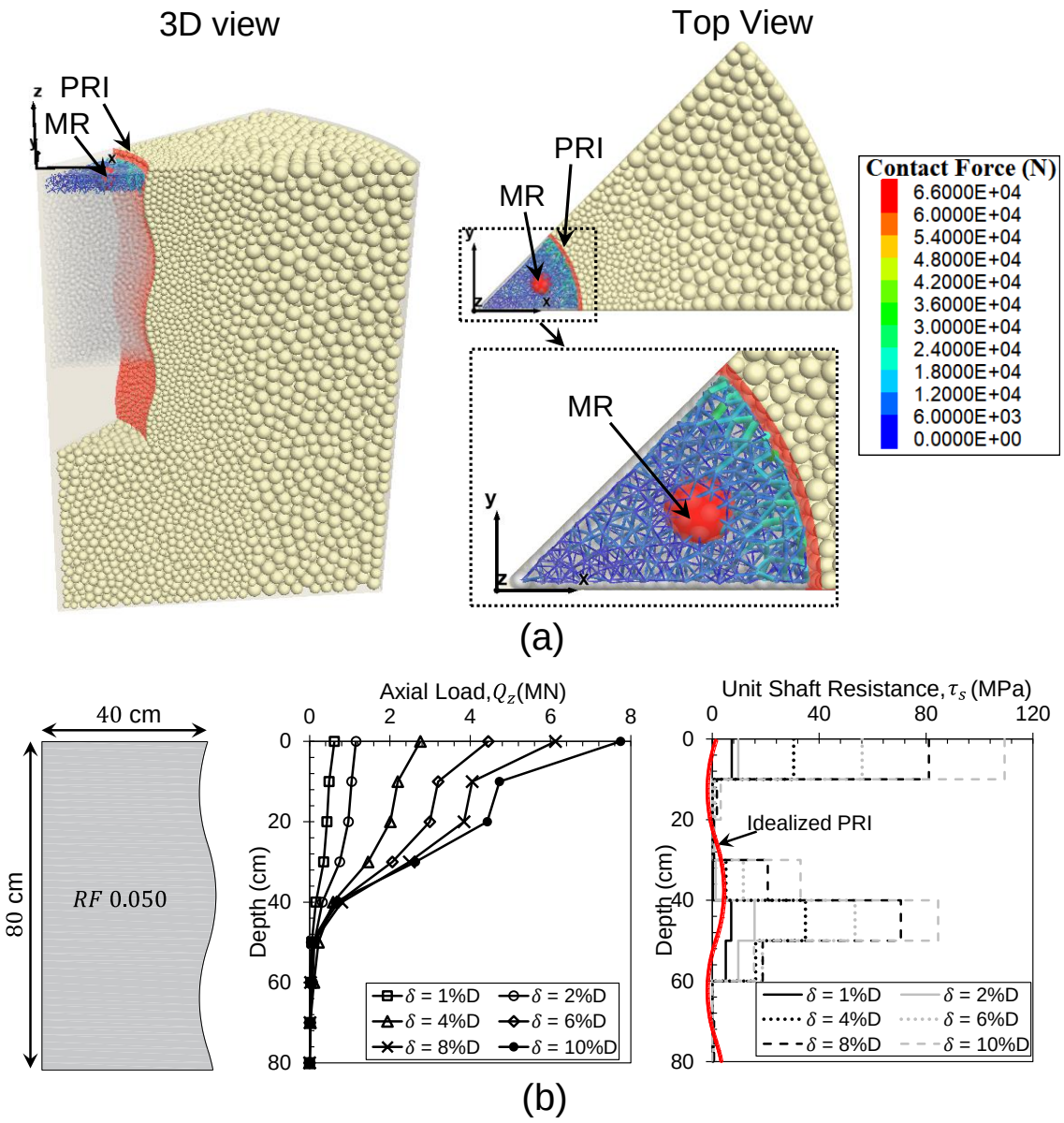


**Fig. 12.** Shortcomings of using MRs to record axial stresses along the pile (model with $RF = 0.050$): Axial load ($Q_z$) and unit shaft resistance ($\tau_s$) distribution vs depth produce the unrealistic result that $Q_z$ decreases at depths where $\tau_s \sim 0$.

These observations are due to the “arching effect” reported herein in Section 3.3.1, in which most of the load transfer from the pile to the surrounding rock occurs at the front of the upper and lower asperities and in which negligible shaft forces mobilize at the back of the asperities, due to the “gap” that is formed at their interface when the pile settles.

### 3.4 Failure mechanism

Next, the failure mechanism of a “rough” RSP is analyzed. To facilitate the illustration and discussion, the RSP with $RF = 0.085$ is used as an example. The analysis was conducted until a $\delta = 20\%D$ is reached; thus, all theoretical stages of the load-settlement response –i.e., pre-peak, peak and post-peak behavior– are covered with the analyses, allowing for full development of the failure mechanism along the pile shaft.

**Fig. 13**–**Fig. 14** illustrate the evolution of damage along the pile, its relationship with the loading process, and the development of the failure mechanism. In particular, **Fig. 13** illustrates how the load-settlement relationship is related to “damage”, measured as the number of cracks that develop within the pile and within the rock in DEM model. Similarly, **Fig. 14** illustrates the failure mechanism. In particular, the “color images” of the first column (**Fig. 14**(a1)-(f1)) illustrate the formation of “gaps” at the back of asperities, and the presence of heavily compressed areas at their front; similarly, it shows pieces of “rock rubble” that are “expelled” from the top and bottom of the pile due to the degradation of asperities at PRI (Xu et al., 2020). (To illustrate this behavior, the rock and pile particles at PRI have been highlighted with blue and green color, respectively; the black surface in transparency represents the initial interface). The magnitudes of particle displacements are shown in **Fig. 14**(a2)-(f2). The initial contact network and the damage evolution (along a section plane crossing the central radial line) during the loading process are shown in **Fig. 14**(a3)-(f3) (grey color represents the initial bonded contacts; blue and red colors represent bond breakage under shear and tensile failure modes, respectively; to facilitate

visualization, note that the initial bonded contacts are plotted transparent for $\delta > 0$). Also, idealized schematic representations derived from **Fig. 14**(1)-(3) are shown in **Fig. 14**(a4)-(f4).

At the beginning of loading (e.g., for $\delta \leq 1\%D$), only a few bonds have broken (see **Fig. 13** and **Fig. 14**(b3-b4)), suggesting that a sliding mechanism with little asperity damage is dominant. After such settlement threshold, damage initiates at the PRI and the number of cracks within the model starts to increase steadily (see **Fig. 13** and **Fig. 14**(b4)).

Then, for larger subsequent settlements –e.g., for $\delta = 5\%D$– the damage evolves as follows: (i) gap zones develop, (ii) initial wedges A and B (light gray regions in **Fig. 14**(c4)) are formed; and (iii) bonds continue to break, mostly concentrated in both asperities (see **Fig. 13** and **Fig. 14**(c3)).

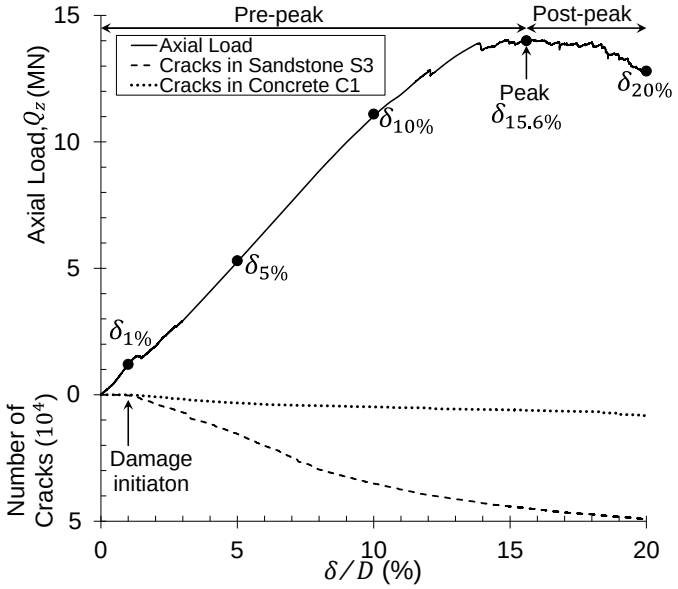


**Fig. 13.** Axial load and number of cracks - settlement response for RSP with $RF = 0.085$.

With further loading (e.g., for $\delta = 10\%D$), the upper gap zones increase their size (see **Fig. 14**(c3-d3)) while interface damage increases further (see **Fig. 14**(d1)-(d4)).

The shearing process also continues, so that wedges A and B increase their size and deform, and a potential extension of the shear band from wedge A to wedge B is observed (red dotted line in **Fig. 14**(d4)).

The peak load is reached for $\delta = 15.6\%D$ (see **Fig. 13**), and by then an extended interface damage is noted, where: (i) a crushed zone is observed close to the socket head (see **Fig. 14** (e1)-(e4)), (ii) the upper asperity starts to shear-off, (see **Fig. 14**(e3)-(e4)), (iii) wedges A and B merge, forming a new (larger) wedge C (see **Fig. 14**(e4)), and (iv) the number of bond breakages and the damage zone size continue to increase (see **Fig. 13** and **Fig. 14**(c4)).

Finally, for $\delta = 20\%D$, a gradual reduction of the pile load capacity (of about 7%) is obtained (see **Fig. 13**), and further interface damage occurs (see **Fig. 14**(f1)-(f4)). At this stage, subsequent shearing at the interface leads to rock rubble being expelled from the lower part of wedge C (see **Fig. 14**(f1)-(f4)). Also, the size of wedge C increases further, and the upper and lower asperities are sheared-off (see **Fig. 14**(f3-)(f4)). Therefore, the failure mechanism described may be affected by the "void" base of the pile considered herein; such rock rubble would not be expelled from a pile with its base resting on the rock.

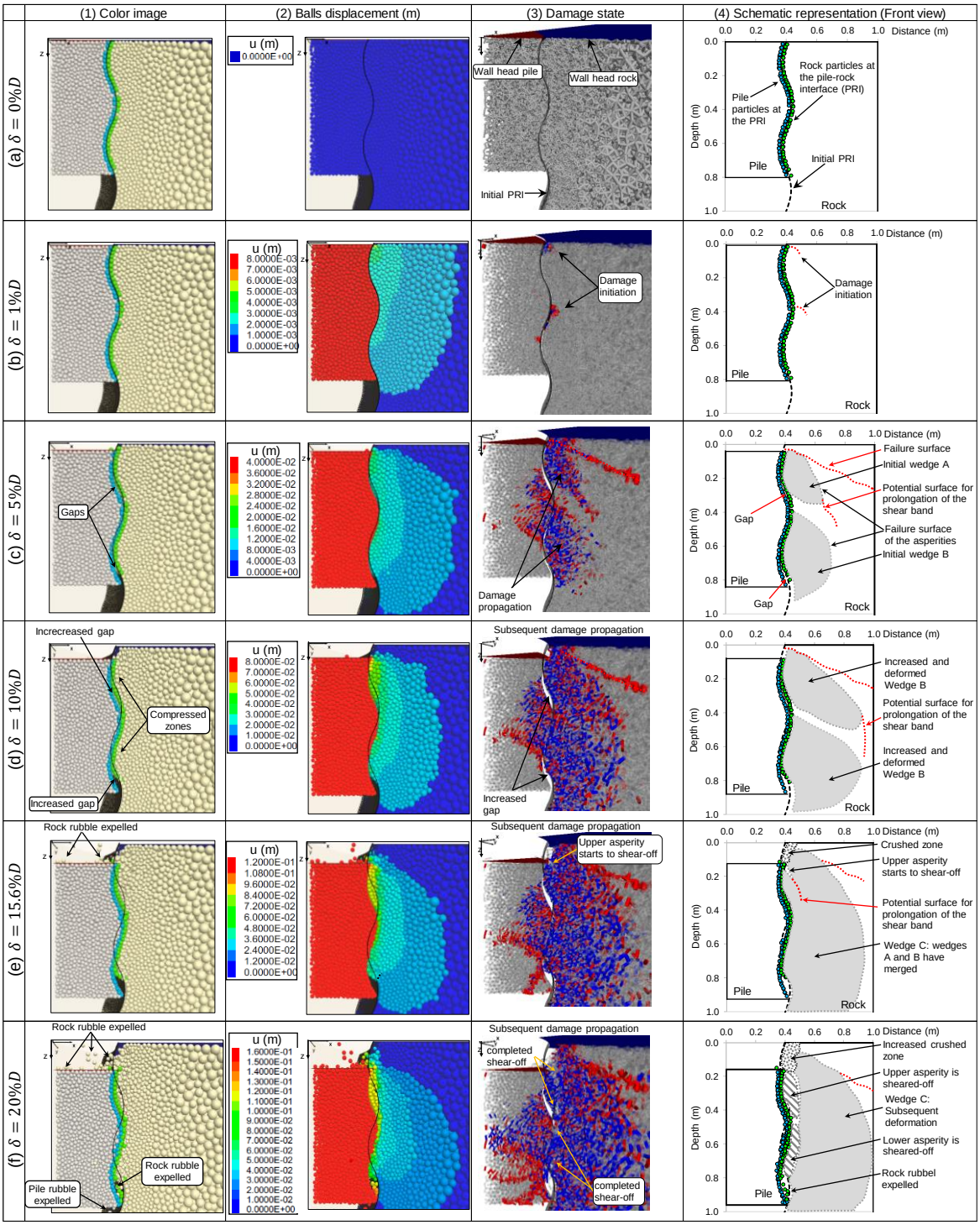


**Fig. 14**. Failure mechanism of a rough RSP (example for pile with $RF = 0.085$).

460 ### 3.5 Comparison with data published by others

461 This section compares the LTM derived from this research with results published by
462 others. To do that, the distribution of the mobilized $Q_z$ with the normalized depth (i.e.,
463 the socket depth divided by its nominal length) is considered, and the RSP with $RF =$
464 $0.025$ is employed for the discussion. The data employed for comparison is
465 summarized in **Table 4** and the corresponding results are shown in **Fig. 15**. It can
466 be observed that the LTM obtained from DEM models developed herein is similar to
467 that reported in the centrifuge tests conducted by Gutiérrez-Ch et al. (2021b), as well
468 as to that from the full-scale load tests conducted by Horvath et al. (1983) and Skejić
469 et al. (2022). This finding is particularly significant and supports the idea that the
470 DEM models developed herein allow for an adequate illustration of the LTM of rough
471 RSPs that had not been previously reported in the literature.

472 **Table 4.** Data of axially loaded RSPs considering shaft resistance only

| Type of test | $\boldsymbol{D}$ (m) | $\boldsymbol{L}$ (m) | $\boldsymbol{RF}$ | Rock type | $\boldsymbol{\sigma_c}$ (MPa) | Reference |
|---|---|---|---|---|---|---|
| DEM test | 0.8 | 0.8 | 0.025 | Sandstone | 21.77 | This work |
| Centrifuge test | 0.8 | 4 | 0.025 | Pseudo-rock | 1.14 | Gutiérrez-Ch et al. (2021b) |
| Full-scale load test | 0.71 | 1.37 | 0.033 | Shale | 5.4 – 5.6 | Horvath et al. (1983) |
| | 0.9 | 3 | 0.021 | Conglomerate | 7.5 | Skejić et al. (2022) |

473

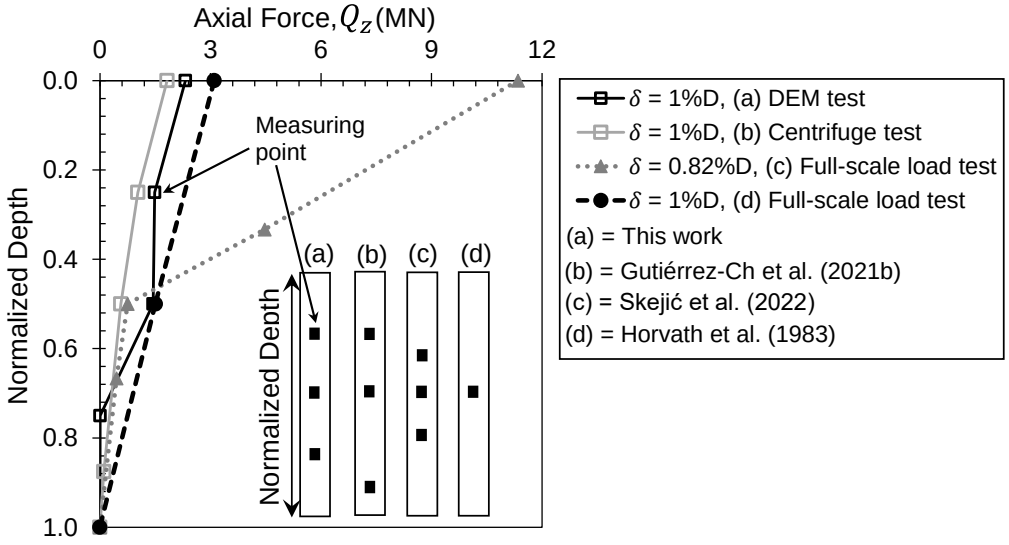


474

475 **Fig. 15**. Comparison of $Q_z$ computed from DEM models with data published by others.

476 ## 4. Conclusions

477 Socket roughness is one of the main factors affecting the behavior of RSPs. This
478 work presents an in-depth analysis of RSP shaft load transfer mechanism,
479 considering different degrees of socket roughness at the PRI. To that end, 3D DEM
480 numerical simulations have been conducted, whose results have been interpreted in
481 the light of an “arching effect”, which governs the transfer of shaft load from the pile
482 to the surrounding rock. Additionally, numerical results are interpreted in the light of
483 previous works on this topic, demonstrating that DEM results reproduce well overall
484 trends reported by others.

485 Numerical results demonstrate that the 3D DEM models developed can analyze the
486 LTM of RSPs with different degrees of socket roughness. In particular, such models
487 can compute: (i) pre-peak, peak and post-peak load-settlement response, (ii) the
488 load-transfer mechanism and its associated distributions of shaft resistance with
489 depth, and (iii) the associated failure modes, which depend on settlement level.

Furthermore, DEM results provide evidence of an “arching effect” that controls the LTM from the pile to its surrounding rock, particularly for rougher piles. This finding is particularly significant, since it goes beyond typical interpretation models of axial load and uniform shaft resistance mobilization with depth. Hence, socket roughness is a key factor that affects LTM of rough RSPs and, therefore, the associated distribution of pile loads with depth.

These DEM results are employed to propose an idealized load-transfer mechanism of RSPs that considers shaft resistance only and socket roughness (see **Fig. 16**), and that integrates ideas previously published by others (Hassan and O’Neill 1997) with the behavior observed by DEM simulations in this study. The initial condition and the components of a typical asperity (i.e., the front, the back and the root of the asperity) before loading are shown in **Fig. 16**(a). During initial loading, or when the pile behavior is still mainly elastic (i.e., for a pile settlement of $\delta \cong 1\%D$, see **Fig. 16**(b)): (i) only compressive stresses exist along the PRI, (ii) the pile transfers load from its head, through an “arching effect”, to the front of asperities of the surrounding rock, so that an unloaded region is noted in the lower portion of the pile, and (iii) gaps develop at the back of asperities, leading to a relaxation of stresses therein. Then, as pile loads continue to increase leading to elastoplastic deformations (i.e., for a pile settlement of $\delta \gg 1\%D$, see **Fig. 16**(c)): (i) the transmission of loads from the pile to the rock due to arching effects continues, (ii) the PRI is deformed, and (iii) the rock asperities are sheared-off and major cracks are noted. The idealized stress path associated to the proposed LTM is presented in **Fig. 16**.

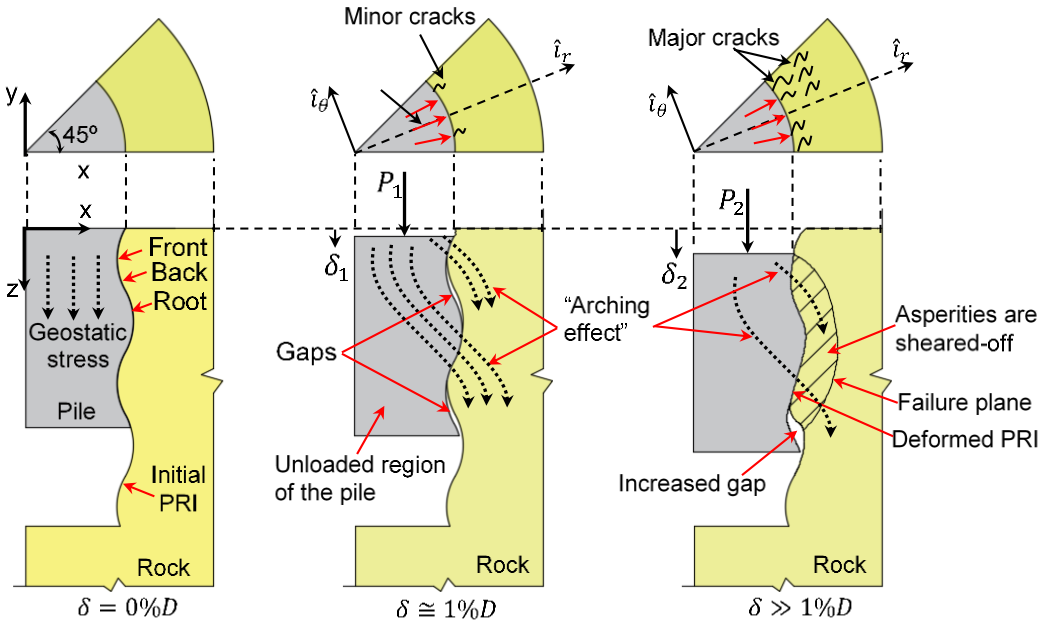


**Fig. 16.** Summary of the idealized LTM for RSPs considering socket roughness: (a) initial condition and components of a typical asperity before loading, (b) elastic loading state, (c) plastic loading state and failure mechanism.

## 5. Data Availability Statement

Some or all data, models, or code that support the findings of this study are available from the corresponding author upon reasonable request.

## 6. Acknowledgements

This research was funded by the Spanish Ministry of Science and Innovation, MCIN/AEI/10.13039/501100011033, under Grant No. PID2019-108060RB-I00. The support of this institution is gratefully acknowledged.

## 7. References

[1] Bahaaddini, M., Sharrock, G., Hebblewhite, B.K., 2013. Numerical direct shear tests to model the shear behavior of rock joints. Comput. Geotech. 51, 101-115. https://doi.org/10.1016/j.compgeo.2013.02.003.

[2] Basarkar, S.S., Dewaikar, D. M., 2006. Load transfer characteristics of socketed piles in Mumbai region. Soils Found. 46(2), 247–257. https://doi.org/10.3208/sandf.46.247.

[3] Dai, G., Salgado, R., Gong, W., Zhu, M., 2016. The effect of sidewall roughness on the shaft resistance of rock-socketed piles. Acta Geotech. 12(2), 429–440. https://doi.org/10.1007/s11440-016-0470-8.

[4] Gu, X.F., Seidel, J.P., Haberfield, C.M., 2003. Direct shear test of sandstone-concrete joints. Int. J. Geomech. 3, 21–33. https://doi.org/10.1061/(ASCE)1532-3641(2003)3:1(21).

[5] Gutiérrez-Ch J.G. 2020. Análisis del efecto de la rugosidad en el contacto roca-pilote sobre la resistencia por fuste de pilotes. PhD Thesis (In Spanish). Universidad Politécnica de Madrid. Spain. https://doi.org/10.20868/UPM.thesis.63589

[6] Gutiérrez-Ch, J.G., Melentijevic, S., 2016. Análisis numérico del efecto de la rugosidad en el contacto pilote-roca sobre la resistencia por fuste y punta (In Spanish). Ingeniería Civil 182, 41–53. http://ingenieriacivil.cedex.es/index.php/ingenieria-civil/article/view/446.

~~[7] Gutiérrez-Ch J.G., 2020. Análisis del efecto de la rugosidad en el contacto roca-pilote sobre la resistencia por fuste de pilotes. PhD Thesis (In Spanish).~~

~~Universidad Politécnica de Madrid. Spain. https://doi.org/10.20868/UPM.thesis.63589.~~

~~[8]~~[7] Gutiérrez-Ch, J.G., Senent, S., Melentijevic, S., Jimenez, R., 2018. Distinct element method simulations of rock-concrete interfaces under different boundary conditions. Eng. Geol. 240, 123–139. https://doi.org/10.1016/j.enggeo.2018.04.017.

~~[9]~~[8] Gutiérrez-Ch JG, Melentijevic S, Senent S, Jimenez, R (2019) DEM models to predict side shear resistance of rock-socketed piles considering socket roughness. 53rd U.S. Rock Mechanics/Geomechanics Symp, 23–26 June: ARMA 19–1757. New York City, New York.

~~[10]~~[9] Gutiérrez-Ch, J.G., Song, G., Heron, C., Marshall, A., Jimenez, R., 2020a. Centrifuge modelling of shaft resistance of a rock-socketed pile. Proc., 4th European Conference on Physical Modelling in Geotechnics-ECPMG, 06–08 September, Lulea, Sweden.

~~[11]~~[10] Gutiérrez-Ch, J.G., Melentijevic, S., Senent, S., Jimenez, R., 2020b. Distinct element method simulations of rock-socketed piles: estimation of shaft resistance considering socket roughness. J. Geotech. Geoenviron. Eng. 143(12): 04020133. https://doi.org/10.1061/(ASCE)GT.1943-5606.0002394.

~~[12]~~[11] Gutiérrez-Ch, J.G., Senent, S., Melentijevic, S., Jimenez, R., 2021a. A DEM-based factor to design rock-socketed piles considering socket roughness. Rock Mech. Rock Eng. 54:3409–3421. https://doi.org/10.1007/s00603-020-02347-1.

~~[13]~~[12] Gutiérrez-Ch, J.G., Song, G., Heron, C., Marshall, A., Jimenez, R., 2021b. Centrifuge tests on rock-socketed piles: effect of socket roughness on shaft resistance. J. Geotech. Geoenviron. Eng. 147(11): 04021125. https://doi.org/10.1061/(ASCE)GT.1943-5606.0002665.

~~[14]~~[13] Hassan, K.M., O'Neill, M.W., 1997. Side load-transfer mechanisms in drilled shafts in soft argillaceous rock. J. Geotech. Geoenviron. Eng. 123(2), 145–152. https://doi.org/10.1061/(ASCE)1090-0241(1997)123:2(145).

~~[15]~~[14] Horvath, R.G., Kenney, T.C., Kozicki, P., 1983. Methods for improving the performance of drilled piers in weak rock. Can. Geotech. J. 20(4), 758–772. https://doi.org/10.1139/t83-081.

~~[16]~~[15] Itasca Consulting Group Inc., 2014. PFC Manual, Version 5.0. (Minneapolis, Minnesota).

~~[17]~~[16] Johnston, I.W., Lam, T.S.K., Williams, A.F., 1987. Constant normal stiffness direct shear testing for socketed pile design in weak rock. Géotechnique, 37(1), 83–89. https://doi.org/10.1680/geot.1987.37.1.83.

[18][17] Kodikara, J.K., Johnston, I.W., 1994. Shear behavior of irregular triangular rock-concrete joints. Int J Rock Mech Min Sci Geomech Abstr 31: 313–322. https://doi.org/10.1016/0148-9062(94)90900-8.

[19][18] Krounis, A., Johansson, F., Larsson, S., 2016. Shear strength of partially bonded concrete-rock interfaces for application in dam stability analyses. Rock Mech. Rock Eng. 49(7), 2711–2722. https://doi.org/10.1007/s00603-016-0962-8.

[20][19] Melentijevic, S., Olalla, C., 2014. Different FEM models for simulation of the Osterberg load test in rock shafts. ISRM Regional Symp. EUROCK 2014. London, United Kingdom.

[21][20] Murali, A.K., Tran, K.M., Haque, A., Bui, H.H., 2022. Experimental and numerical investigation of the load-bearing mechanisms of piles socketed in soft rocks. Rock Mech. Rock Eng. 55, 5555–5576. https://doi.org/10.1007/s00603-022-02954-0.

[22][21] Ng, C. W.W., Yau, T.L.Y., Li, J.H.M., Tang, W.H., 2001. 'Side resistance of large diameter bored piles socketed into decomposed rocks.' *J. Geotech. Geoenviron. Eng.* 127(8), 658–669. https://doi.org/10.1061/(ASCE)1090-0241(2001)127:8(642).

[23][22] O'Neill, M.W., Townsend, F.C., Hassan, K.M., Buller, A., Chan, P.S. 1996. Load transfer for drilled shafts in intermediate geomateriales. U.S. Department of Transportation, FHWA-RD-95–172, Final Report.

[24][23] Pells, P.J.N., Rowe, R.K., Turner, R.M., 1980. An experimental investigation into side shear for socketed piles in sandstone. Proc., Int. Conf. on Struct. Found. on Rock 1, 291-302. Sydney, Australia.

[25][24] Rajan, P.M., Krishnamurthy, P., 2019. Termination criteria of bored pile subjected to axial loading. Indian Geotech. J. 49(5), 566–579. https://doi.org/10.1007/s40098-019-00359-5.

[26][25] Rowe, R.K., Armitage, H.H., 1987. A design method for drilled piers in soft rock. Can. Geotech. J. 24(1), 126–142. https://doi.org/10.1139/t87-011.

[27][26] Seidel, J.P., Collingwood, B., 2001. A new socket roughness factor for prediction of rock socket shaft resistance. Can. Geotech. J. 38 (1), 138–153. https://doi.org/10.1139/t00-083.

[28][27] Seidel, J.P., Haberfield, C.M., 1995. The axial capacity of pile sockets in rocks and hard soils. Ground Eng. 28(2), 33–38.

[29][28] Skejić, A., Gavrić, D., Jurišić, M., Rahimić, Đ., 2022. Experimental and numerical analysis of axially loaded bored piles socketed in a conglomerate rock

mass. Rock Mech. Rock Eng. 55, 6339–6365. https://doi.org/10.1007/s00603-022-02932-6.

~~[30]~~[29] Whitaker, T., Cooke, R.W., 1966. An investigation of the shaft and base resistances of large bored piles in London Clay. Proc Symp of Large Bored Piles, 7-49. London, UK.

~~[31]~~[30] Williams, A.F., Pells, P.J.N., 1981. Side resistance in sandstone, mudstone, and shale. Can. Geotech. J. 18(4), 502–513. https://doi.org/10.1139/t81-061.

~~[32]~~[31] Xu, J., Haque, A., Gong, W., Gamage, R.P., Dai, G., Zhang, Q., Xu, Feng., 2020. Experimental study on the bearing mechanisms of rock-socketed piles in soft rock based on micro X-ray CT analysis. Rock Mech. Rock Eng. 53, 3395–3416. https://doi.org/10.1007/s00603-020-02121-3.

~~[33]~~[32] Zhao, X., Shen, Y., Melentijevic, S., Sun, Z., Wang, K., Xu, J., Li, Z., 2024. The load-bearing mechanism of rock-socketed piles considering rock fragmentation. Rock Mech. Rock Eng. https://doi.org/10.1007/s00603-024-04041-y.